Received: 12 January 2022 | Revised: 9 August 2022 | Accepted: 19 August 2022

DOI: 10.1002/mrm.29448

RESEARCH ARTICLE

Magnetic Resonance in Medicine

CEST MR Fingerprinting (CEST-MRF) for Brain Tumor Quantification Using EPI Readout and Deep Learning Reconstruction

Ouri Cohen[1] | **Victoria Y. Yu**[1] | **Kathryn R. Tringale**[2] | **Robert J. Young**[3] | **Or Perlman**[4,5,6] | **Christian T. Farrar**[4] | **Ricardo Otazo**[1,3]

[1]Department of Medical Physics, Memorial Sloan Kettering Cancer Center, New York, New York, USA

[2]Department of Radiation Oncology, Memorial Sloan Kettering Cancer Center, New York, New York, USA

[3]Department of Radiology, Memorial Sloan Kettering Cancer Center, New York, New York, USA

[4]Athinoula A. Martinos Center for Biomedical Imaging, Department of Radiology, Massachusetts General Hospital and Harvard Medical School, Charlestown, Massachusetts, USA

[5]Department of Biomedical Engineering, Tel Aviv University, Tel Aviv, Israel

[6]Sagol School of Neuroscience, Tel Aviv University, Tel Aviv, Israel

Correspondence
Ouri Cohen, Memorial Sloan Kettering Cancer Center, 320 East 61 St, New York, NY 10025, USA.
Email: coheno1@mskcc.org

Funding information
European Union, Grant/Award Number: 836752; NIH/NCI, Grant/Award Numbers: P30-CA008748, R37CA262662-01A1

Purpose: To develop a clinical CEST MR fingerprinting (CEST-MRF) method for brain tumor quantification using EPI acquisition and deep learning reconstruction.

Methods: A CEST-MRF pulse sequence originally designed for animal imaging was modified to conform to hardware limits on clinical scanners while keeping scan time under 2 min. Quantitative MRF reconstruction was performed using a deep reconstruction network (DRONE) to yield the water relaxation and chemical exchange parameters. The feasibility of the six parameter DRONE reconstruction was tested in simulations using a digital brain phantom. A healthy subject was scanned with the CEST-MRF sequence, conventional MRF and CEST sequences for comparison. Reproducibility was assessed via test–retest experiments and the concordance correlation coefficient calculated for white matter and gray matter. The clinical utility of CEST-MRF was demonstrated on four patients with brain metastases in comparison to standard clinical imaging sequences. Tumors were segmented into edema, solid core, and necrotic core regions and the CEST-MRF values compared to the contra-lateral side.

Results: DRONE reconstruction of the digital phantom yielded a normalized RMS error of $\leq$7% for all parameters. The CEST-MRF parameters were in good agreement with those from conventional MRF and CEST sequences and previous studies. The mean concordance correlation coefficient for all six parameters was 0.98 ± 0.01 in white matter and 0.98 ± 0.02 in gray matter. The CEST-MRF values in nearly all tumor regions were significantly different ($P = 0.05$) from each other and the contra-lateral side.

Conclusion: Combination of EPI readout and deep learning reconstruction enabled fast, accurate and reproducible CEST-MRF in brain tumors.

KEYWORDS
chemical exchange rate, chemical exchange saturation transfer (CEST), deep learning, DRONE, magnetic resonance fingerprinting (MRF), pH

1 | INTRODUCTION

CEST MRI uses frequency selective radiofrequency pulses to saturate the magnetization of labile protons on proteins and metabolites.[1] The saturated protons exchange with the unsaturated water protons and lead to a measurable reduction in the water MRI signal. The CEST contrast is attractive since it is sensitive to metabolite concentrations with higher spatial resolution (~1 mm) and shorter scan times (~5 min) than MRS.[2] Moreover, the measured CEST signal depends, inter alia, on the chemical exchange rate, which is pH sensitive. Because many pathologies, including cancer, are characterized by tissue hypoxia leading to an acidic microenvironment, pH is a potentially valuable metabolic biomarker.[3–6] In cancer imaging, CEST contrast has been used to distinguish pseudoprogression and radiation necrosis from true progression in brain tumors,[7–9] quantify tumor extracellular pH,[3,10] evaluate the grading and cellularity of gliomas,[11] and monitor early effects of radiation therapy.[12]

Although preclinical and early clinical CEST studies have demonstrated the potential utility of CEST methods for assessing disease pathologies, disease progression, and therapeutic response, they have not been widely adopted for clinical use due to several challenges encountered in clinical translation. Specifically, the semi-quantitative nature of the CEST contrast, the relatively long image acquisition times, and the complicated data processing have all hindered clinical translation. To overcome these challenges, MR fingerprinting (MRF)-based CEST was recently introduced[13,14] and demonstrated in vivo for rat brain experiments on a preclinical 4.7T scanner.[15] The CEST-MRF sequence has the following advantages over conventional CEST: tissue maps are fully quantitative; the acquisition time is short (less than 2 min) and the data analysis is greatly simplified because only a single resonance frequency offset is excited with saturation pulses of varying powers (instead of the full Z-spectrum) which also reduces the sensitivity to B0 variations due to the use of a normalized signal. Accuracy of the tissue parameter maps was validated in phantoms and compared to reference methods from the literature.[16–19]

The diagnostic potential of CEST-MRF for pathologies is considerable since the resulting parametric maps reflect different biophysical processes, and their combination provides a comprehensive picture of complex pathologies, like brain tumors, where multiple parameters change simultaneously. However, to realize the clinical potential of CEST-MRF, the pulse sequence must be adapted to clinical scanners. This is challenging because preclinical scanners have significantly different RF and gradient amplifier capabilities and limitations compared to clinical scanners. For example, patient imaging is bound by strict limits on specific absorption rate and peripheral nerve stimulation. These hardware and software differences require careful consideration when adapting a sequence for clinical use. An additional challenge inherent to CEST-MRF is the large number of tissue parameters quantified by the sequence. In conventional MRF, tissue quantification is achieved by pattern-matching the measured signal to a pre-computed database of signal magnetizations.[20] However, the exponential growth in dictionary size for multiple tissue parameters renders this approach impractical for CEST-MRF. Some groups have reported the use of a MRF framework with a two-pool model in healthy subjects to quantify the water and semi-solid parameters but not the pH-sensitive amide exchange.[21,22] Others have proposed to sequentially quantify the semi-solid and CEST parameters using dictionary matching (DM) reconstruction necessitating two separate scans and a potentially lengthy reconstruction process.[23]

The aim of this work is to develop CEST-MRF acquisition and quantification methods suitable for clinical scanners to image patients with brain metastases. Specifically, a combination of MRF with EPI readout and deep learning-based quantification is proposed. The proposed method is tested in simulations and a healthy volunteer and validated in vivo against conventional CEST imaging. The clinical utility is demonstrated in patients with metastatic brain cancer.

2 | METHODS

2.1 | Pulse sequence

Figure 1A shows the proposed pulse sequence for one temporal point of the acquisition schedule. Subsequent temporal points of the acquisition schedule use the same pulse sequence but with different CEST saturation encoding (Figure 1B). The initial pulse train saturates the solute protons and is composed of 160 non-selective, Gaussian-shaped, 16 ms sub-pulses applied with a 100% duty cycle for a total pulse train duration (T_{sat}) of 2560 ms. The saturation pulse train power ($B1_{sat}$) was varied according to a pre-determined schedule as described in Section 2.1.1. The resonance frequency of the RF pulses was set to the chemical shift of the amide protons (3.5 ppm) in this study but protons of other moieties (amine, hydroxyl, etc.) are easily probed by setting the resonance frequency to the appropriate chemical shift. The saturated protons chemically exchange with the unsaturated bulk water protons which leads to a reduction in the water signal which can be measured by excitation with an on-resonance RF pulse with flip angle (FA) set according to the MRF acquisition schedule. The magnetization

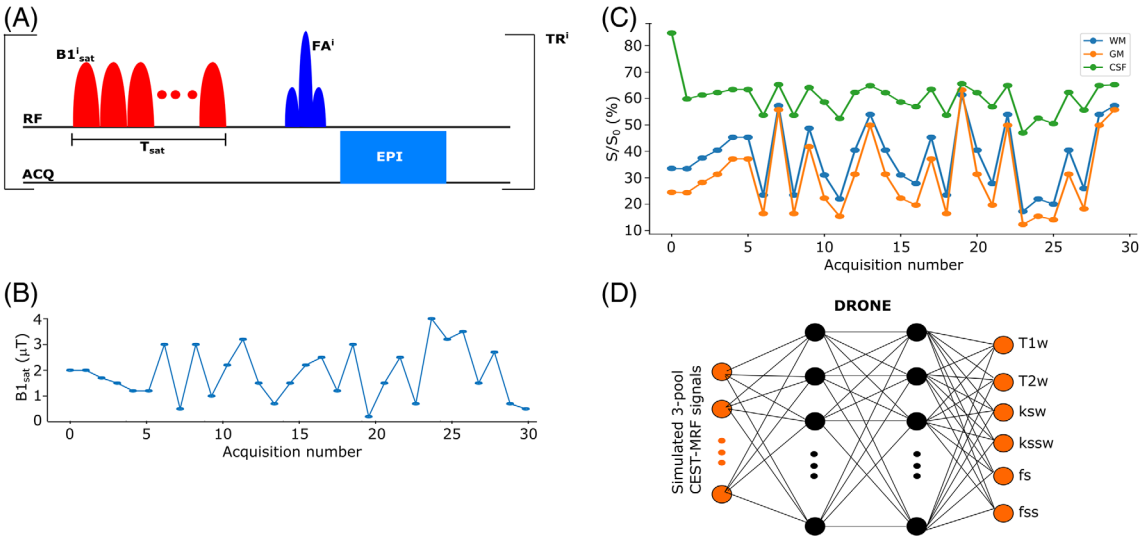

FIGURE 1 (A) Clinical CEST-MRF pulse sequence shown for one schedule point. The magnetization is saturated with a Gaussian-shaped pulse train and exchanges with the water. The water signal is then excited and read out with an EPI k-space sampling. The saturation pulse train power ($B1_{sat}$) and duration (T_{sat}) and the excitation pulse FA are varied according to the MRF acquisition schedule. For simplicity, only the saturation power was varied in this study. (B) Schedule of $B1_{sat}$ powers. (C) Sample CEST-MRF signals for GM, WM and CSF. (D) DRONE network used in quantification of the CEST-MRF data. The network is trained with simulated three-pool data and outputs the water relaxation ($T1_w$, $T2_w$), amide (ksw, fs), and semi-solid (kssw, fss) parameters

is then sampled with an EPI readout and the acquisition repeated, following a repetition delay (TR), for each point in the acquisition schedule.

2.1.1 | MRF acquisition schedule

To ensure a differential signal evolution for different tissues and facilitate their quantification, the acquisition parameters must be varied for each schedule point. Although simultaneous variation of multiple acquisition parameters can improve discrimination and reduce acquisition times,[24] the choice of an appropriate schedule is a challenging problem,[25] and will be explored in future studies. For simplicity, in this work $B1_{sat}$ was randomly varied for 30 schedule points with powers in the range 0-4μT (Figure 1B), which was found to yield accurate parameters in previouspreclinical in vivo studies.[15] The variable saturation gives rise to a differential tissue evolution for different tissue types (Figure 1C). All other acquisition parameters (FA, TR, T_{sat}) were kept constant with FA set to 90°, TR set to 3500 ms, and T_{sat} set to 2560 ms.

2.2 | Deep learning-based tissue parameter quantification

In conventional MRF, tissue parameters are quantified by matching the measured signal to a pre-computed dictionary of signal magnetizations. Because of the large number of tissue parameters (dictionary dimensions) and the exponential growth of the dictionary, this approach is infeasible for CEST-MRF. We have previously demonstrated the use of a model-trained neural network named DRONE[26–30] to perform a functional mapping between the measured data and the underlying tissue parameters. In this work, we extended the DRONE approach to enable reconstruction of the high-dimensional CEST-MRF signals in a clinical setting. The benefits of DRONE include nearly instantaneous reconstruction time and the use of signal simulation to train the network which removes the need of patient data for training. The neural network used in this work was also trained on simulated data, as in the original DRONE method, but in this case training data were generated by solving the Bloch-McConnell equations for a three pool (water, solute, semi-solid) model.

2.2.1 | Training dataset generation

The neural network was implemented in PyTorch[31] and consisted of a 30-node input layer (corresponding to the 30-point magnitude images acquired with the CEST-MRF sequence), two fully connected hidden layers with 300 nodes per layer, and a six-node output layer (Figure 1D). The output layer corresponded to the six parameters measured by the CEST-MRF sequence consisting of water T1 relaxation ($T1_w$), water T2 relaxation ($T2_w$),

amide exchange rate (ksw), amide volume fraction (fs), semi-solid exchange rate (kssw), and semi-solid volume fraction (fss). A training dataset was generated by sampling the tissue parameter ranges using latin hypercube sampling[32] and simulating a CEST-MRF acquisition by solving the Bloch-McConnell equations. All signals were normalized to have a l_2-norm of 1. The transmit field inhomogeneity (B1) was included in the training dictionary, but not in the loss calculation, to induce the network to minimize the error in the other parameters instead. To accelerate the training set generation, the CEST-MRF simulation was implemented on a Nvidia RTX2080 Ti graphics processing unit (Nvidia Corp. Santa Clara, CA) with 11 GB of memory, which enabled parallel processing of the training set entries. A fraction (20%) of the dataset was used as a validation set to assess the quality of network training with the remainder (80%) used for training. The network was trained for 4000 epochs with the Adam optimizer[33] using an l1-norm loss with a batch size of 1000 and an adaptive learning rate with weight decay of 10^{-4}. Zero-mean Gaussian noise with 1% SD was added to the training dictionary to promote robust learning.

2.3 | Numerical simulations

Sensitivity to parameter values

The sensitivity of CEST-MRF to different parameter values was tested by synthesizing CEST spectra for WM and GM with the CEST-MRF derived parameters. Baseline values were defined for the tissue parameters and spectra were synthesized using twice and half the baseline values. The difference between the baseline spectrum and those synthesized with the other parameter values was calculated along with the Pearson correlation and the RMS error (RMSE). The same experiment was then repeated but with synthesized CEST-MRF fingerprints for the baseline and modified parameter values. Simulations were performed numerically stepwise under the assumption of a Lorentzian MT lineshape.

DRONE analysis

The feasibility of DRONE reconstruction for six parameter maps was assessed in a custom modified Brainweb-based[34] digital phantom. The segmented gray matter (GM), white matter (WM), and CSF phantom maps were used to assign quantitative values, representative of the healthy brain, for each tissue type and parameter (Supporting Information Table S1, which is available online). The digital phantom was used to simulate a CEST-MRF acquisition with the sequence and acquisition schedule described in Section 2.1. The simulated data were reconstructed using a DRONE network trained with a training set of 60 000 entries sampled from the ranges shown in Supporting Information Table S2 as well as using DM. The error between the reconstructed tissue parameter and the reference values was calculated as Error = 100 × |Reference – Reconstructed|/Reference.

White Gaussian noise was added to the simulated data to study the effect of noise on the reconstruction for varying levels of SNR. The SNR was defined as $20\cdot\log_{10}(S/N)$, where S was the average WM signal intensity for the acquisition and N was the noise SD. The SNR was varied from 20 to 80 dB in intervals of 5 dB,[35] and the data reconstructed with the same network for each SNR level. The normalized RMS error (NRMSE), defined as $NRMSE = 100 \times \sqrt{\left\{\sum_i \left(Estimated_i - Reference_i\right)^2\right\}}/\overline{Reference}$ where $\overline{Reference}$ is the mean of '*Reference*', was used to calculate the error between the estimated and reference values for the different SNR levels.

We tested the stability of the DRONE reconstruction by creating a numerical phantom with 128 × 128 points. Each point had a constant ksw and fs (40 Hz and 0.5% respectively). The other parameters ($T1_w$, $T2_w$, kssw, fss, and B1) were randomly varied by selection from the ranges shown in Supporting Information Table S2. The phantom was used to simulate a CEST-MRF acquisition, and the resulting fingerprints reconstructed by the DRONE network to obtain the estimated tissue parameters. The RMSE, mean ± SD, and reconstruction error, calculated as above, were computed for the ksw and fs parameters. The contribution of the other parameters to the reconstructed ksw and fs values was quantified by multiple regression.

To test the self-consistency of the DRONE reconstruction, measured in vivo data was reconstructed with a trained DRONE network (as described in Section 2.4) or DM. The tissue parameter maps were converted to a digital phantom and used to generate fingerprints in a simulated CEST-MRF acquisition. The simulated data was then reconstructed with the same DRONE network or DM and the error between the initial and iterated reconstruction calculated. This was repeated for 40 iterations.

The DRONE network nonlinearly maps the input signal to the underlying tissue parameters. To quantify the impact of the input on the resulting tissue parameters, we calculated an 'attribution score' for sample WM and GM fingerprints using the Integrated Gradients method.[36,37]

2.4 | In vivo studies

All experiments were conducted on a 3T GE Signa Premier (GE Healthcare, Waukesha, WI) with the built-in transmit body coil and a head coil array with 48 elements for reception.

2.4.1 | Healthy volunteer subject

A healthy 34-y-old female volunteer was recruited for this study and provided informed consent in accordance with our institution's Institutional Review Board protocol. The subject was scanned with the CEST-MRF sequence described in Section 2.1 with the following image acquisition parameters: FOV = $280 \times 280\,mm^2$, matrix size = 256×256, in-plane resolution = $1.1 \times 1.1\,mm^2$, slice thickness = 5 mm, TE = 24 ms, partial Fourier, number of averages (NEX) = 1, TR = 3500 ms, FA =90°, T_{sat} = 2560 ms, bandwidth = 250 kHz. The total scan time was 105 s. The measured data was reconstructed with the same network defined in Section 2.3. The SNR for the in vivo acquisition, calculated as described in Section 2.3, was approximately 53 dB.

Sensitivity to B0 inhomogeneity

A B0 map was acquired using a dual-echo gradient echo sequence to assess the impact of B0 inhomogeneities on the CEST-MRF parameters. Seven regions-of-interest (ROI) were selected corresponding to areas with B0 values in a 50 Hz range. The correlation between the tissue parameter values and the B0 values in the ROIs was calculated for each parameter.

In vivo reproducibility

The in vivo reproducibility of the CEST-MRF sequence was assessed by test–retest scanning. The healthy volunteer was sequentially scanned twice with the CEST-MRF sequence and then removed from the scanner. Following a 5-min delay, the subject was again placed in the scanner, re-localized and scanned two more times with the CEST-MRF sequence. Data from each scan were reconstructed with the trained DRONE network and GM and WM ROIs defined. The ROIs were then used to determine the GM and WM values for all parameter maps. The Lin's concordance correlation coefficient (CCC)[38] was calculated in the GM and WM of each tissue parameter as a measure of the reproducibility of each parameter.

Comparison with conventional MRF derived T1 and T2 maps

The water T1 and T2 relaxation maps obtained with CEST-MRF were compared to an optimized conventional MRF-EPI sequence.[26,35] The imaging parameters were kept the same as the CEST-MRF acquisition with the exception of the initial adiabatic inversion pulse with inversion time of 50 ms which preceded the data acquisition.[20] The acquired data were processed by a separate DRONE network and the total acquisition time for the optimized 50-point schedule was approximately 6 s per slice. The GM/WM ROIs defined in Section 2.4.1.2 were used to calculate the reference mean ± SD T1 and T2 values.

Comparison with conventional CEST imaging

Validation of the CEST-MRF parameters is difficult because no reference method is available. Instead, CEST spectra were synthesized from the CEST-MRF parameters and compared to experimentally measured spectra in the same subject. The subject was scanned with a CEST sequence with 57 resonance frequency offsets in the −7.2 to 7.2 ppm range. The FA, $B1_{sat}$, TR, and T_{sat} were set to 90°, 2 μT, 8, and 3.04 s respectively. Unlike CEST-MRF, T1 effects are not accounted for in conventional CEST so a long TR was chosen to ensure complete signal recovery and avoid possible T1 contamination between measurements. Similarly to other studies,[39] both the synthetic and measured spectra were normalized to the magnetization at a saturation offset of 7.2 ppm to ensure a fair comparison and eliminate the need for correcting motion-induced misregistration between the M0 image and the spectra. The total scan length for the CEST acquisition was 7.6 min. The same acquisition parameters were used along with the CEST-MRF derived parameters as inputs to a Bloch-McConnell equation simulator to generate the synthetic spectra and the Pearson correlation between the two curves calculated.

To isolate the CEST signal from the significantly larger water and magnetization transfer (MT) signals, the measured Z-spectrum ($Z_{Measured}$) was compared to a synthetic reference spectrum calculated using the water and MT parameters alone ($Z_{SynthRef}$). The RMSE of the difference $Z_{Measured} - Z_{Synthetic}$ was calculated for WM and GM.

Comparison with dictionary fitting

The performance of the DRONE network for the in vivo data was compared to standard dot-product pattern matching with a dictionary composed of 4 million entries generated using the parameter ranges listed in Supporting Information Table S2.

2.4.2 | Patients with brain metastases

Four patients with brain metastases were recruited for this study and gave informed Institutional Review Board consent. The patients were scanned per the consensus standardized brain tumor imaging protocol[40] and institutional standard-of-care that included T1-weighted sequences pre- and post-gadolinium (Gd) contrast injection, FLAIR, diffusion, and perfusion acquisitions. All patients were previously treated with radiation

therapy and/or chemotherapy. The proposed CEST-MRF was acquired prior to Gd injection using the same imaging parameters and tissue quantification as for the healthy volunteer scans (Section 2.4.1) other than the resolution which was set to $1 \times 1 \times 3\,mm^3$ to enable visualization of small lesions. The tumor was contoured into ROIs comprising a necrotic core, solid core, and edema as well as a contra-lateral healthy region by one of the authors (K.R.T.), a trained radiation oncologist. Statistical significance of differences in the reconstructed tissue map values for each ROI in a representative patient (patient 1) was evaluated using a multi-comparison analysis of variance test with Tukey honest significant difference[41] with a significance level set at $P = 0.05$.

3 | RESULTS

3.1 | Computation time

Deep learning quantification using DRONE significantly reduced the quantification time compared to conventional DM. Conventional dictionary generation and matching required approximately 4 h on a desktop server with 256 GB of memory. Network training required approximately 30 min on a graphics processing unit, whereas quantification of the six parameter maps with the trained network required only ~100 ms for an image with 256×256 voxels.

3.2 | Numerical simulations

The DRONE reconstruction of the six tissue parameter maps in the simulated digital phantom is shown in Figure 2 for a high SNR simulation (80 dB) to isolate the intrinsic error in the DRONE reconstruction for the highly under-determined CEST-MRF data. DM results are shown in Supporting Information Figure S1. The impact of SNR on the quantitative accuracy for each parameter is shown in Figure 3A on a log–log scale. Despite the high dimensionality of the data and the small training dictionary, the DRONE reconstruction accurately quantified the tissue maps yielding a NRMSE of less than 7% for all the parameters. As expected, increasing SNR reduced the NRMSE for all tissue parameters although the rate of improvement varied for each parameter which is reflective of the intrinsic sensitivity of the sequence to the different parameters. As an example, the NRMSE at 55 dB was approximately 8% for fss but 3% and 6% for $T1_w$ and $T2_w$. The attribution score for each schedule point is shown in Figure 3B. The first and last schedule points were found to have the highest impact on the resulting maps. The sensitivity of the CEST-MRF parameters is illustrated in Supporting Information Figures S2 and S3.

The DRONE stability experiments yielded for ksw a RMSE of 6.1 Hz, Mean ± SD of −1.0 ± 6.0 Hz, and error of 12.4%. The overall regression was statistically significant with $R^2 = 0.762$ and $F(16\,384, 16\,377) = 8740$. For fs the results were: RMSE = 0.11%, Mean ± SD = 0.06 ± 0.09

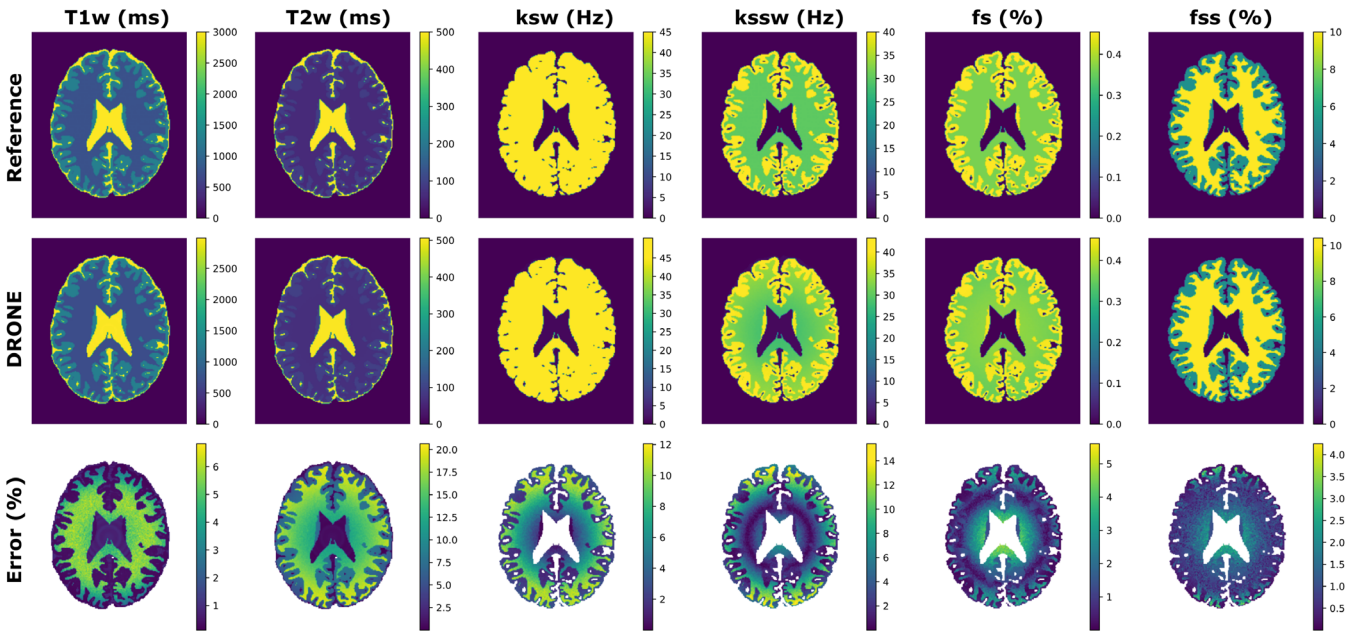

FIGURE 2 DRONE reconstruction of six parameters in a digital phantom in comparison to the reference values. Regions associated with the background, skull, and scalp were set to zero. The error, calculated as 100 × |Reference – DRONE|/Reference, is shown for each tissue. Note the effect of the B1 inhomogeneity visible in the error maps

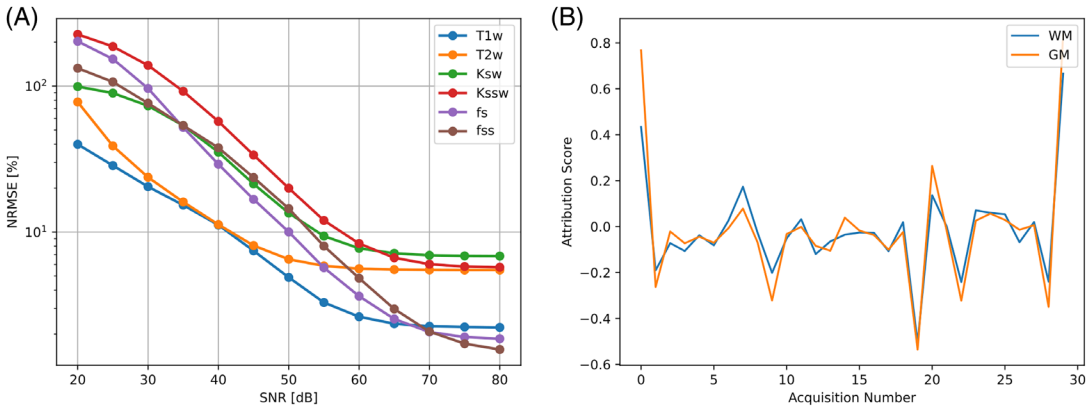

FIGURE 3 (A) NRMSE, on a log scale, of the DRONE reconstructed CEST-MRF maps in a digital brain phantom using a random schedule for varying levels of added white gaussian noise. Changes in SNR non-linearly affected the NRMSE of the different parameters illustrating the sensitivity of the sequence and schedule to each tissue parameter. (B) Attribution score calculated using Integrated Gradients[36,37] for sample WM and GM fingerprints. Note that the first and last point in the acquisition schedule had the greatest impact on the output

and error of 18.6%. The regression was statistically significant with $R^2 = 0.704$ and $F(16\,384,16\,377) = 6479$. The fitted regression model coefficients for ksw and fs are shown in Supporting Information Table S3. The effect of the MT parameters was an order of magnitude smaller than that of other factors illustrating the independence of the CEST parameters. Although not trained for recursive reconstruction, the DRONE reconstruction was nevertheless self-consistent with the error for repeated iterations converging to ~0%, unlike DM, which converged to ~12% error (Supporting Information Figure S4).

3.3 | Healthy human volunteer

The quantitative CEST-MRF tissue parameter maps for the healthy human subject are shown in Figure 4A. The mean and SD of the GM and WM values for each tissue parameter are listed in Table 1 along with the reference water T1 and T2 values obtained with the conventional MRF sequence which are shown in Figure 4B. The mean B0 value across the slice was approximately 4 Hz but varied significantly (approximately Δ0.5 ppm range) near the frontal sinuses and temporal regions, as expected. The tissue parameter changes for varying B0 values are shown in Figure 5A–F. All parameters were essentially uncorrelated with B0 ($R^2 < 0.08$) except for $T2_w$ which was only poorly correlated ($R^2 = 0.33$). This is also evident in the tissue maps of Figure 4 where the susceptibility differences near the sinuses and the EPI readout used gave rise to geometrical distortions apparent in that region but little variations in the CEST-MRF parameters. The dictionary fitted data (Supporting Information Figure S5) yielded tissue maps that were heavily discretized (due to the fixed increment used) and noisier compared to the DRONE output.

3.3.1 | In vivo reproducibility

The mean tissue parameter values for each of the four repeated scans are shown for GM and WM in Figure 6 and the corresponding CCC values are tabulated in Table 1. The repeated scans showed strong reproducibility (CCC >0.93) for all parameters despite uncorrected registration errors induced by patient motion between scans.

3.3.2 | Comparison with conventional CEST

The synthesized CEST curves for representative GM and WM points are shown overlaid on the measured CEST curves in Figure 7A,B. There was overall good agreement between the measured and synthesized curves with a Pearson correlation of 0.98 for both GM and WM. Differences in the curves in the negative offset regions were due to nuclear Overhauser (NOE) effects that were not included in the CEST-MRF model. The RMSE of the measured and synthetic curve ($Z_{Measured}$-$Z_{Synthetic}$), calculated for the positive offsets (excluding the unaccounted NOE effects) was 0.023 for WM and 0.045 for GM. The measured and synthetic Z-spectra are shown in Figure 7C–F for WM and GM with the difference curves showing a notable increase in the amide +3.5 ppm resonance offset.

3.4 | Patients with brain metastases

The CEST-MRF parameter maps for a representative patient are shown in Figure 8A along with the T1-weighted (pre-, post-Gd), FLAIR, diffusion, and perfusion scans

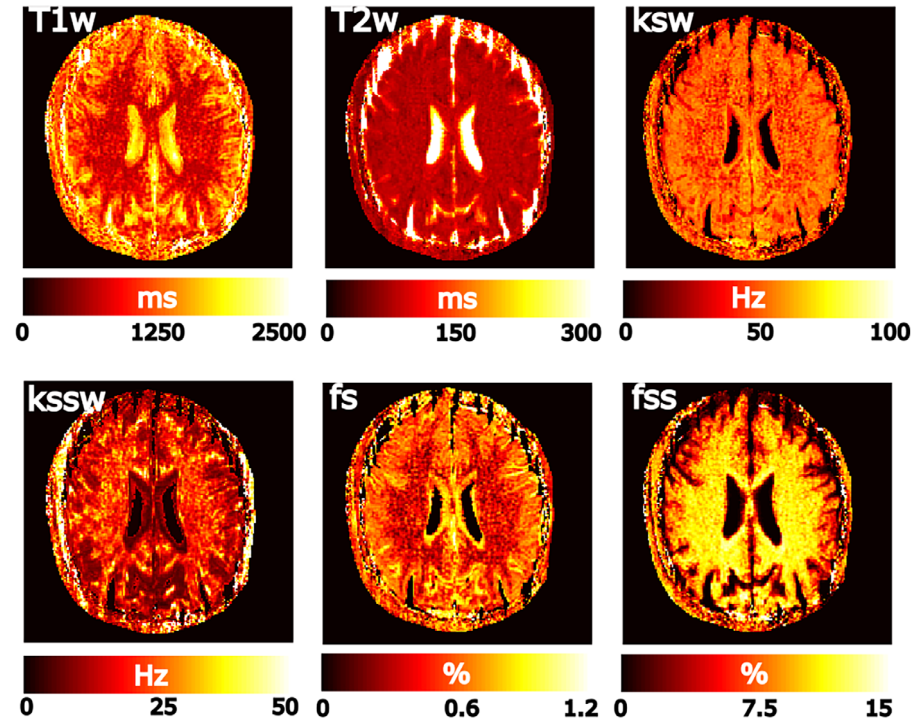

FIGURE 4 (A) Reconstructed tissue parameter maps obtained from a healthy volunteer with the CEST-MRF method. Note the elevated semi-solid volume fraction in the WM reflective of the higher myelin content. (B) Reference T1 and T2 maps obtained with the optimized MRF-EPI sequence

from the standard brain protocol for comparison. The correspondence between the measured fingerprints in the different ROIs and those synthesized from the DRONE reconstructed tissue parameters are shown in Figure 8B. Box and whiskers plots of the CEST-MRF tissue map values for each ROI in the same patient are shown in Figure 8C. The differences between the parameter values in the different ROIs for all tissue parameters were statistically significant ($P = 0.05$) except as shown in Figure 8D. A box and whiskers plot for all patients is shown in Figure 9. There were notable trends in the parameter maps. The $T1_w$ and $T2_w$ in the tumor were both elevated in comparison to the contra-lateral tissue, particularly in the necrotic region. The amide exchange rate in the necrotic region was lower which is suggestive of a lower pH environment. The amide volume fraction was also reduced in the necrotic and edema regions.

4 | DISCUSSION

4.1 | Effect of schedule on quantitative parameters

The CEST-MRF signal depends on multiple acquisition parameters including the shape of the saturation pulses, duration and frequency, the excitation FA, saturation power, and others. The dependence on multiple parameters can be beneficial in improving the discrimination between signals from different tissues. The semi-solid pool can particularly benefit from inclusion of additional resonance frequency offsets in the schedule given the very broad linewidth of the MT pool which would improve kssw discrimination. For simplicity, in this work only the saturation power was varied using a random schedule that is unlikely to be optimal. The numerical phantom

TABLE 1 Estimated CEST-MRF parameter values and CCC for GM and WM in a healthy volunteer

		This study				*Conventional MRF*	*Literature*	
		Mean ± SD	**95% CI**	**CCC**	**95% CI**	**Mean ± SD**	**Mean ± SD**	***Reference***
$T1_w$ (ms)	WM	864 ± 166	[847, 881]	0.9717	[0.9713, 0.972]	821 ± 35	956±217[a]	Bojorquez et al.[43]
	GM	1403 ± 203	[1383, 1423]	0.98399	[0.98378, 0.984]	1527 ± 429	1482±150[a]	
$T2_w$ (ms)	WM	74.0 ± 5.31	[73.4, 74.5]	0.99501	[0.99494, 0.9951]	77.8 ± 7.20	75±3[b]	Lu et al.[44]
	GM	80.6 ± 8.69	[79.8, 81.5]	0.99403	[0.99394, 0.99411]	91.7 ± 28.1	83±4[b]	
ksw (Hz)	WM	48.4 ± 5.09	[47.9, 48.9]	0.99214	[0.99203, 0.9923]		42.3 ± 2.9	Perlman et al.[42]
	GM	50.0 ± 3.84	[49.6, 50.4]	0.99168	[0.99157, 0.99179]		34.6 ± 9.5	
kssw (Hz)	WM	23.6 ± 5.92	[23.0, 24.2]	0.9645	[0.96397, 0.96502]		23 ± 4	Stansiz et al.[45]
	GM	14.3 ± 4.66	[13.8, 14.7]	0.96127	[0.96069, 0.96183]		40.0 ± 1	
fs (%)	WM	0.504 ± 0.098	[0.491, 0.513]	0.96436	[0.96386, 0.96486]		0.31 ± 0.02	Perlman et al.[42]
	GM	0.601 ± 0.057	[0.595, 0.607]	0.98506	[0.98484, 0.98528]		0.32 ± 0.07	
fss (%)	WM	9.83 ± 0.943	[9.74, 9.93]	0.98786	[0.98768, 0.98804]		8.9 ± 0.3	Stansiz et al.[45]
	GM	6.19 ± 1.78	[6.01, 6.36]	0.93658	[0.93572, 0.93744]		4.4 ± 0.4	

[a] Mean of all reported values.
[b] Mean of reported occipital and frontal GM.

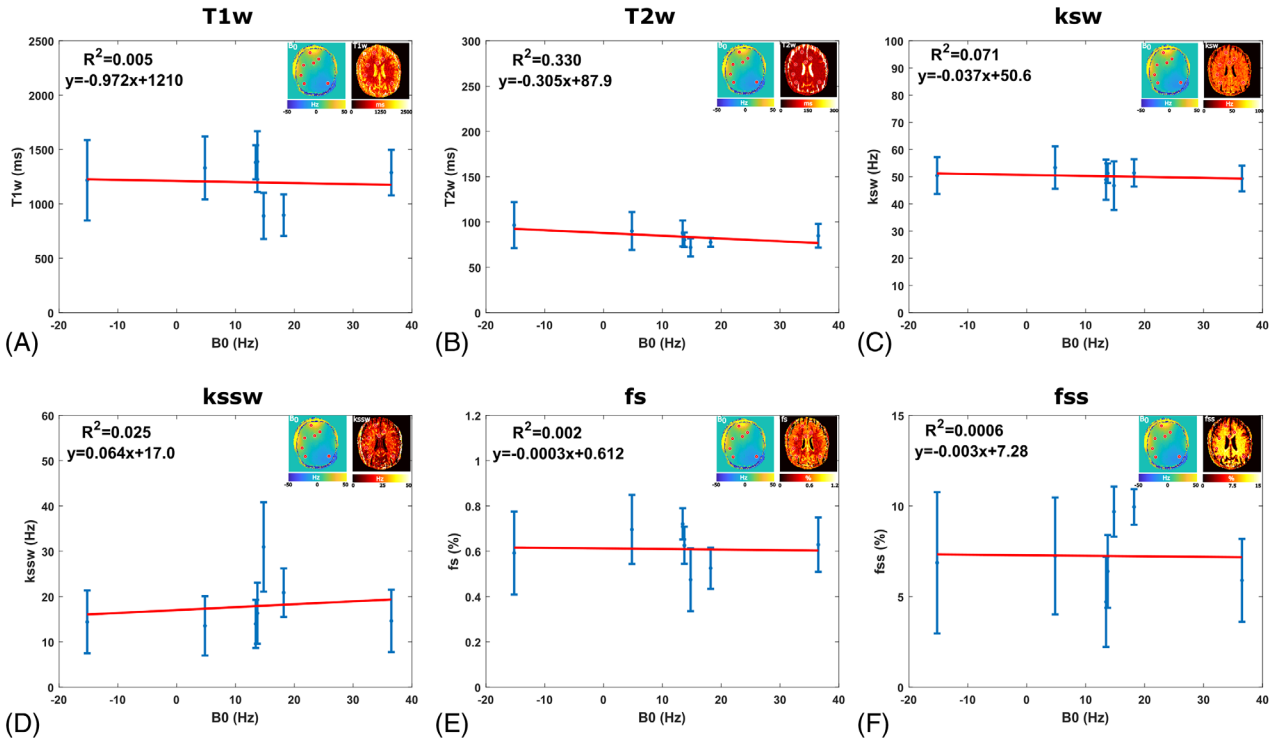

FIGURE 5 Variation in the tissue parameter maps as a function of the B0 inhomogeneity. Shown are the water relaxation parameters: $T1_w$ (A) and $T2_w$ (B); amide parameters: ksw (C) and fs (E); and semi-solid parameters: kssw (D) and fss (F). Note the poor correlation between the B0 values and the different parameters illustrative of the robustness of the sequence to B0 variations

results (Figure 3) exemplify this since increasing the SNR reduced the NRMSE for all tissue parameters, as expected, but the rate of improvement varied by parameter. This reflects the intrinsic sensitivity of the sequence to each parameter which can be optimized by modifying the acquisition schedule. Indeed, work by our group and others has shown that simultaneously varying multiple acquisition parameters and optimizing the acquisition schedule can

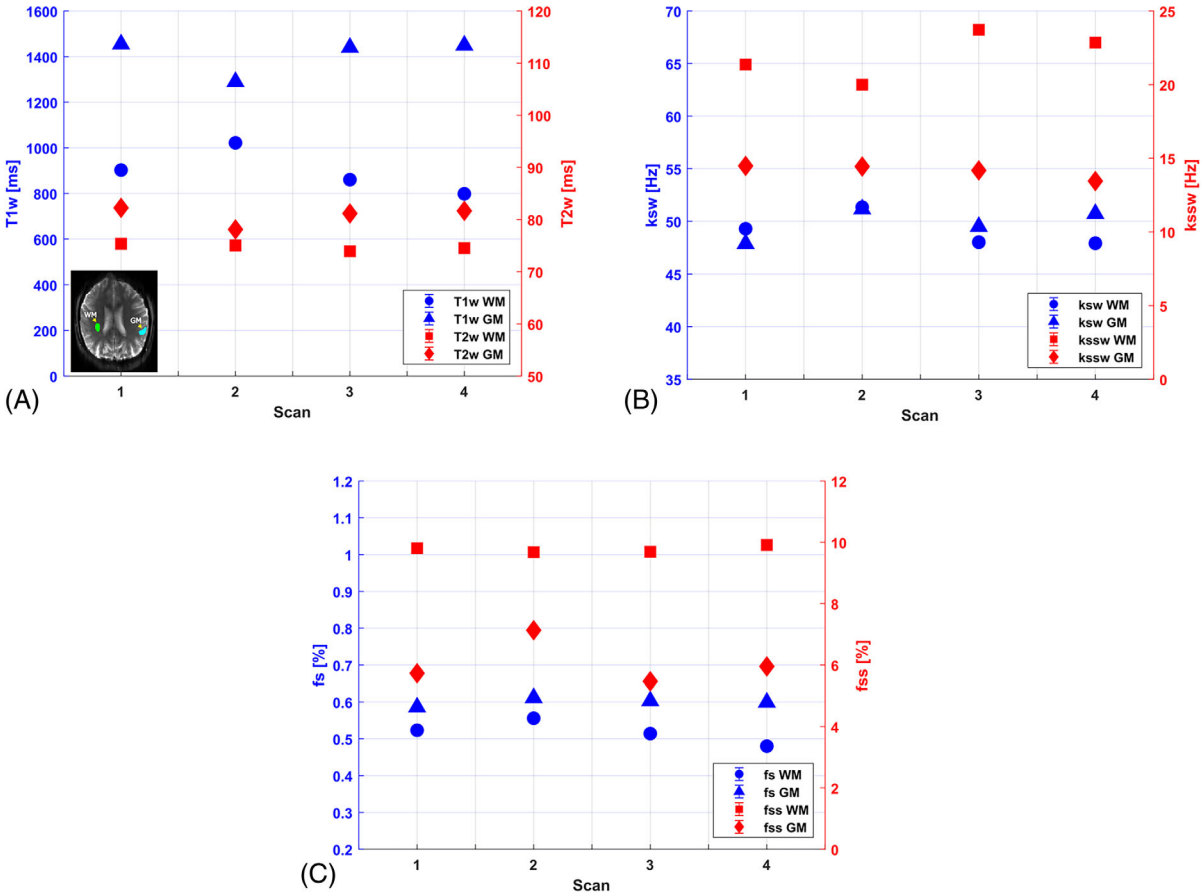

FIGURE 6 In vivo GM and WM tissue parameter values for the four CEST-MRF scans in the healthy volunteer. Scans 1 and 2 were acquired in the first session and scans 3 and 4 in the second session. Blue entries correspond to the left y-axis and red entries to the right y-axis with error bars omitted for clarity. (A) $T1_w$ and $T2_w$. (B) ksw and kssw. (C) fs and fss. The locations of the WM and GM regions used are shown inset in (A). Note the good repeatability between scans. The concordance correlation coefficient for each parameter and tissue type is listed in Table 1

markedly improve tissue discrimination, reduce the sensitivity to noise and shorten the total scan time.[25,35,46–48] However, the optimization of CEST-MRF schedules is challenging because of the large number of parameters (high dimensionality) of the optimization problem. To overcome this difficulty, we have previously introduced a deep learning schedule optimization approach for CEST-MRF optimization and demonstrated it on a preclinical scanner.[24,49] This method can be readily adapted for the clinical CEST-MRF sequence described in this work and is expected to significantly improve the sensitivity to noise and the accuracy of the tissue map quantification. Future work will explore this idea.

4.2 | Neural network reconstruction of high dimensional signals

While the original DRONE was only applied for T1 and T2 mapping,[26] the method is capable of simultaneous estimation of a much larger set of parameters.[28–30,42] Nevertheless, there are important challenges associated with reconstruction of high dimensional signals. First, for the network to correctly estimate the underlying tissue parameters, the training set must adequately cover the parameter space. Unfortunately, due to the "curse of dimensionality," this requires large training datasets and consequently long processing time. To overcome this problem, we used a regular sampling of the parameter space and implemented the training dataset generation on a graphics processing unit to parallelize the processing. This enabled the use of a small (60 000 entries) seven-dimensional dictionary comprising of the six tissue parameters and the instrumental parameter B1. Although the B1 was included in the training dictionary, to avoid the risk of the network converging to spurious solutions given the high dimensionality of the problem, B1 was excluded from the network output and the training error calculation. The network training therefore minimized errors in the tissue parameters alone while still accounting for the inevitable B1 variations in

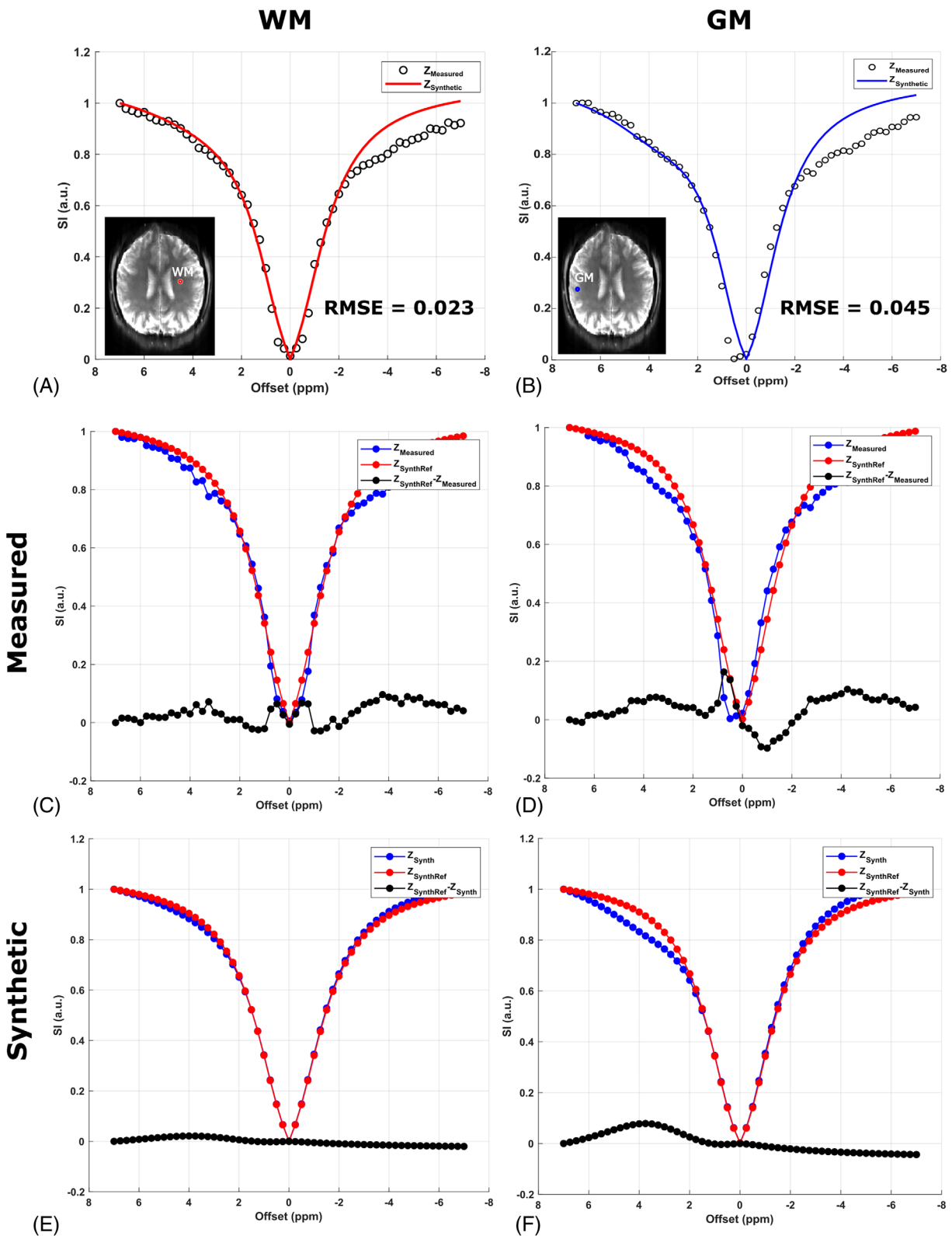

FIGURE 7 Comparison between a measured CEST spectrum and one synthesized from the CEST-MRF parameters for WM (A) and GM (B). Nuclear Overhauser effects, not included in the CEST-MRF model, led to the discrepancy between the curves in the negative offsets' region. The measured and synthetic curves were nevertheless highly correlated (r = 0.98) with an RMSE of 0.023 for WM and 0.045 for GM. A comparison between the measured CEST spectrum and one synthesized from the MT and water parameters alone is shown for WM (C) and GM (D). A comparison between a synthetic CEST spectrum and one including only MT and water parameters is shown for in (E) for WM and in (D) for GM

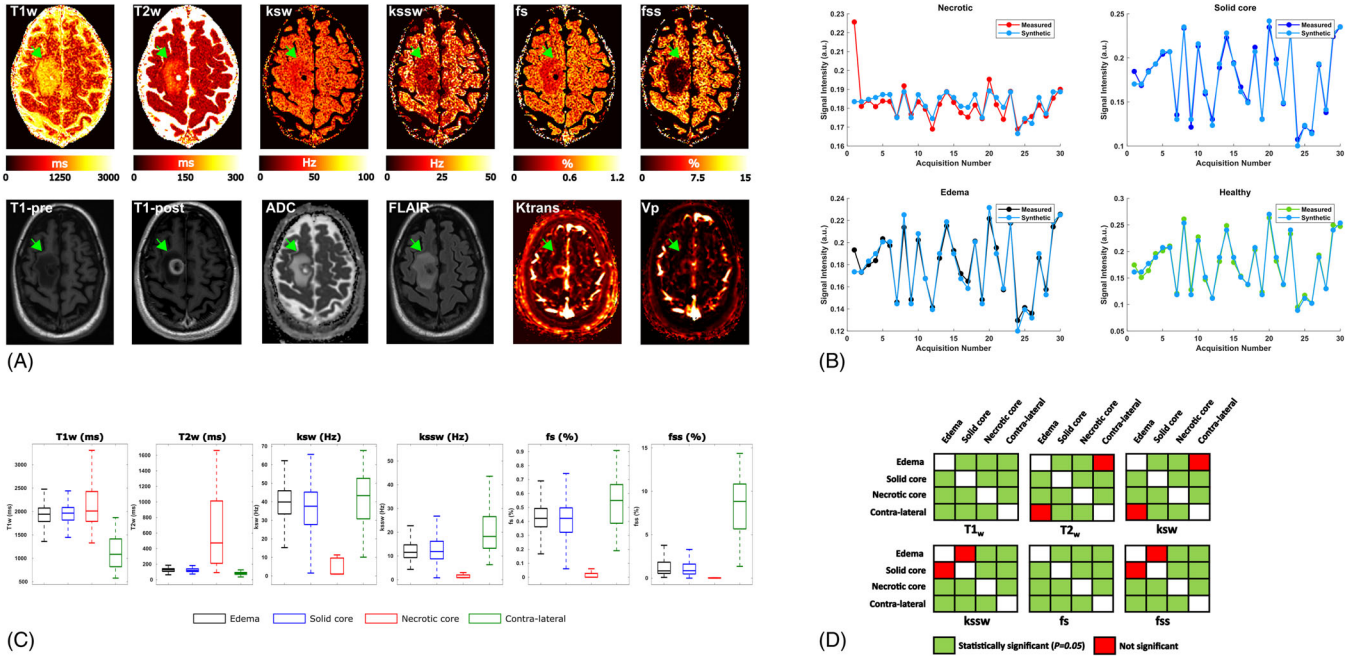

FIGURE 8 (A) In vivo CEST-MRF maps from a patient with brain metastasis and the corresponding images from a standard clinical protocol for comparison. Green arrows indicate the location of the lesion. The segmented tumor regions are denoted by the colored outlines on the $T1_w$ map and include the edema (black), solid core (blue), necrotic core (red), and contra-lateral (green) regions. The T1-pre and T1-post denote the T1-weighted acquisition before and after contrast injection whereas Ktrans and Vp refer to the perfusion and plasma volume maps. The marked differences in the tissue map values between the lesion and healthy tissues are notable. (B) Measured and synthetic fingerprints for different tumor regions. The synthesized fingerprints were calculated from the DRONE reconstructed tissue parameters. Note the agreement between the curves. (C) Box and whiskers plots of the reconstructed tissue maps values for the different ROIs. The distribution of the parameter values along with the median and the first and third quartile ranges are shown. (D) Graphical illustration of the statistical significance of the differences between the various tumor ROI pairs. All regions denoted in green were statistically significantly ($P = 0.05$) as determined by a multi-comparison analysis of variance test with Tukey honest significant difference

vivo. Since T1 estimation is biased by B1, the inclusion of B1 mitigates the T1 underestimation described in prior CEST-MRF studies.[15] Although B0 was not included in the network training, there was only poor correlation between the B0 values and the tissue parameters and little variation in the tissue parameter values across the measured slice (Figure 4), despite significant susceptibility differences near the sinuses. This illustrates the intrinsic robustness to B0 inhomogeneity of the CEST-MRF pulse sequence combined with the DRONE reconstruction. The insensitivity of the CEST-MRF method to B0 shifts results from the use of a fixed saturation frequency offset and the normalization of the trajectory by the trajectory norm. If the saturation pulse is spectrally localized within the relatively broad amide proton resonance, shifts in the irradiation position caused by B0 field inhomogeneity will only result in a different scaling of the signal trajectory for a given voxel, which will be normalized out when taking the norm of the trajectory. However, more severe B0 inhomogeneity that may be encountered in future 3D whole brain studies may need to be addressed by including B0 in the training dictionary as was done for B1.

4.3 | In vivo studies

There was generally good agreement between the tissue parameter values obtained with the CEST-MRF sequence and alternative methods. While there is a wide range of reported values in the literature, the mean WM and GM $T1_w/T2_w$ measured in this study (Table 1) agreed with both the reference conventional MRF values as well as literature values from multiple studies using a variety of different quantification techniques.[43] Optimizing the schedule to improve the T1 discrimination (by additionally varying FA and TR, for instance) and refining the network's B1 estimation may address this issue but further study is needed to confirm this. The mean amide exchange rates measured in this study (WM/GM = $48.4 \pm 5.09/50.0 \pm 3.84$ Hz) were similar to that measured in vivo with CEST-MRF in preclinical[15,42] and clinical[23] models and with spectroscopic methods.[19] Slight differences were observed between the WM/GM parameters measured in this study and those of Perlman et al.[42] These may be due to the two-step acquisition they used where an initial MT-tailored schedule isolated the MT parameters that were then used to

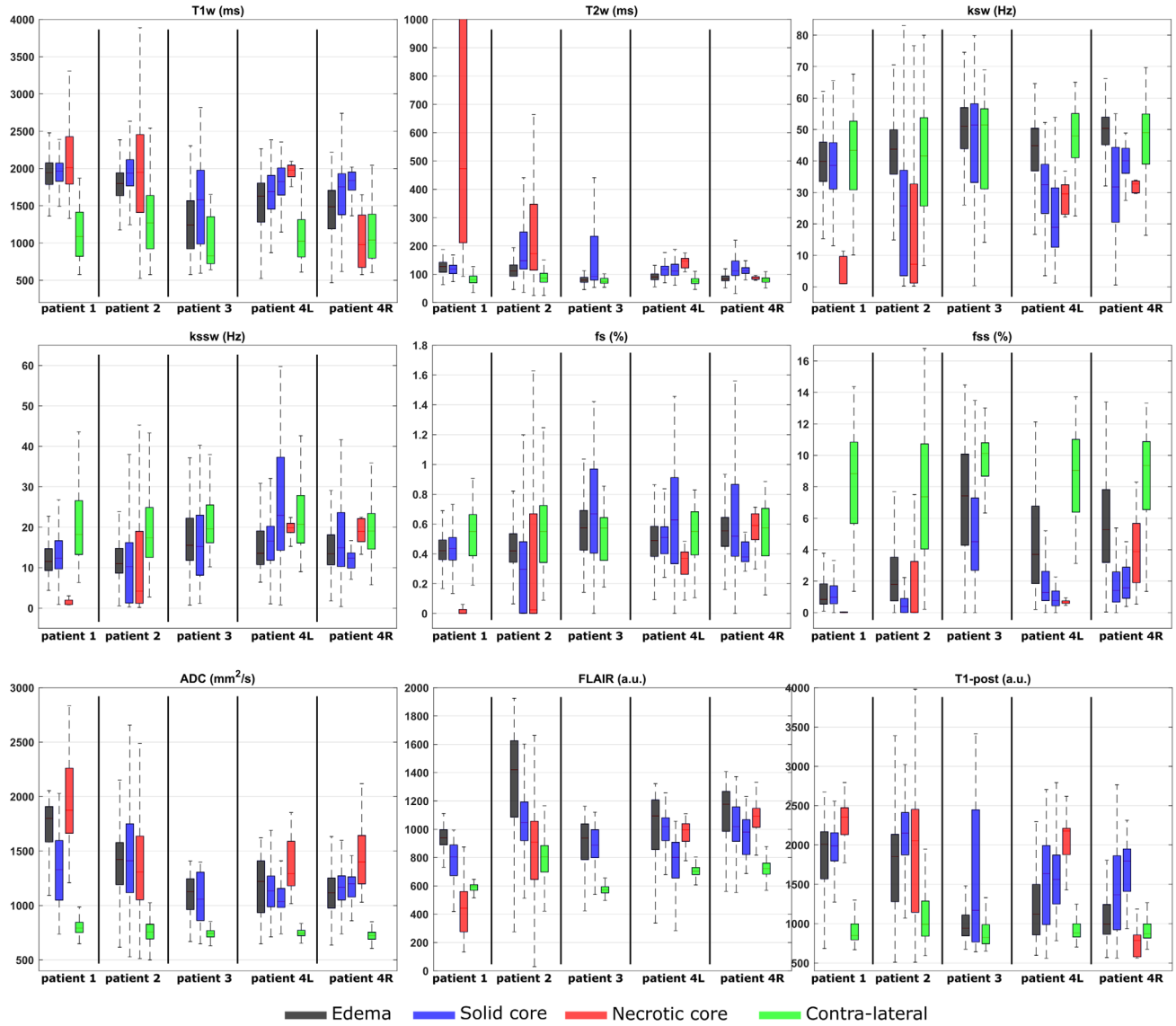

FIGURE 9 Box and whiskers plots for CEST-MRF-derived T1, T2, ksw, kssw, fs, and fss as well as conventional sequence values from T1 post Gd contrast, ADC, and FLAIR images. Patient #1: 61-y-old male, non-small cell lung cancer adenocarcinoma, Patient #2: 65-y-old female, melanoma, Patient #3: 48-y-old female non-small cell lung cancer adenocarcinoma/small cell, Patient #4: 40-y-old male, melanoma (L: left side with two tumors and surrounding region. R: right side with two tumors and surrounding regions)

obtain the CEST parameters. In our method, a single acquisition is performed to obtain all parameters. Further study would be required to compare both approaches. Some studies have found higher amide exchange rates in healthy subjects in vivo (WM/GM = ~162/~365 Hz).[13] Given that pH is similar in WM and GM in the healthy brain[50] and since the amide proton pool is from mobile proteins whose chemical environment is water, WM and GM should also have the same amide base catalyzed exchange rate constant. The stark differences between WM/GM were explained by the authors as arising from the spread of in vivo amide exchange rates[13] although a lack of discrimination in the acquisition schedule or limits in the nonlinear fitting used may have contributed as well. There was a clear delineation between GM and WM in the fss map which is expected given the high WM myelin content and the sensitivity of the semi-solid volume fraction to lipid content. In general, validating the CEST-MRF parameters is difficult because no gold-standard exists for all parameters. As an alternative, a CEST spectrum synthesized from the CEST-MRF parameters was compared to a measured CEST spectrum in vivo. The agreement between the two spectra ($r = 0.98$) is indicative of the accuracy of the reconstructed CEST-MRF maps though there were some differences between the measured and synthetic spectra in the negative offset region of the spectrum. This is understandable given that NOE effects, arising from aliphatic protons with chemical shifts between −2

and −5 ppm, were not included in the CEST-MRF model but are present in the experimentally measured CEST spectrum. The test–retest experiments (Figure 6, Table 1) demonstrate the strong reproducibility of the CEST-MRF tissue maps, despite potential uncorrected subject motion. Further work is necessary to confirm the reproducibility, which is a critical feature for longitudinal studies or treatment response monitoring applications for this technology.

4.4 | Brain tumor studies

The significantly different values between the drawn tumor ROIs (Figure 8C, Figure 9) can improve tumor segmentation and may provide more specific tumor characterization. While previous studies[51,52] have shown hyper-intense CEST signals in tumors, which seemingly differ from the ksw and fs values obtained in this study, this discrepancy can be attributed to multiple confounding factors present in conventional CEST, as described in a recent review.[53] Specifically, in many tumors, changes to the tissue parameters occur simultaneously hyperintense CEST signals can be caused by the changing tumor water relaxation which are typically unaccounted for.[54] Correcting for this effect can eliminate the hyperintensity.[55] In contrast, the combination of the CEST-MRF maps allows separation of different contributors to the signal thus improving tumor characterization. Tumors can also exhibit hyper- or hypo-intense CEST signals depending on the presence of hemorrhage, large vessels, or liquefactive or coagulative necrosis[56] so histopathology is needed for a definitive determination. It should be noted that the lesion shown in Figure 8 is one that was previously irradiated which is sure to affect the CEST-MRF maps. This is also evident in the perfusion (Ktrans, vp) maps (Figure 8A) which are suggestive of a treated tumor. This may explain the similarity between the edema and solid core regions on the kssw and fss maps although partial volume effects due to an imperfect segmentation between these neighboring regions could have contributed as well. Some features in the CEST-MRF maps, like the reduced amide volume fraction (fs) in the necrotic and edema regions, can be understood as resulting from disrupted protein synthesis in necrotic cells and diluted protein concentrations due to edema. Similarly, the decreased amide exchange rate in the necrotic core is consistent with a decreased pH as expected for apoptotic and necrotic tumor regions.[57–59] Finally, the reduced semi-solid volume fraction (fss) in the lesion can be a result of demyelination in that region or post-treatment effects. At present, the biological effects of radiation on the CEST-MRF tissue maps are not well understood and represent an additional confounding factor. Furthermore, as demonstrated by the results from multiple patients (Figure 9), brain metastases arising from different primary tumor histologies showed varying parameter values. Because of the intrinsic biological variability in tumors, prospective large-scale studies will be required to draw meaningful conclusions about relationships between the CEST-MRF maps and the associated tumor characteristics.

4.5 | Limitations and future work

In the current version of the acquisition sequence, coverage is limited to a single slice which may be inadequate for tumors with large spatial extent. Incorporating simultaneous multi-slice and/or slice interleaving can resolve this issue without increasing acquisition time, as recently demonstrated.[60] Indeed, an optimized ordering of the slice interleaving can also improve tissue discrimination as previously shown.[61] The availability of a rapid and non-invasive method for imaging endogenous amide exchange rates and pH makes possible many different studies. One example is the imaging of the tumor's response to oncolytic virotherapy, as recently demonstrated in a preclinical model.[42] Such studies will facilitate development of personalized therapies and can help improve treatment outcomes.

5 | CONCLUSION

This is the first study to demonstrate the feasibility and utility of CEST-MRF in clinical cancer imaging using a combination of fast EPI acquisition and deep learning parameter quantification. The proposed CEST-MRF presented good reproducibility and quantitative results that are consistent with conventional qualitative MRI. CEST-MRF can be particularly beneficial in complex pathologies such as brain tumors.

ACKNOWLEDGMENTS

The authors are grateful to Luanna Chan and Tara Fahy for assistance with patient recruitment and to Dr. Tejus Bale for insights into tumor pathology. This work was supported by NIH/NCI grants P30-CA008748 and R37CA262662-01A1. OP acknowledges funding from the European Union's Horizon 2020 research and innovation program under the Marie Skłodowska-Curie grant agreement No 836752 (OncoViroMRI). This paper reflects only the authors' view, and the Research Executive Agency of the European Commission is not responsible for any use that may be made of the information it contains.

CONFLICT OF INTEREST

O.C. and C.T.F. hold patents on the CEST-MRF technology.

ORCID

Ouri Cohen https://orcid.org/0000-0003-3632-8094
Or Perlman https://orcid.org/0000-0002-3566-569X
Ricardo Otazo https://orcid.org/0000-0002-3782-4930

REFERENCES

1. Wu B, Warnock G, Zaiss M, et al. An overview of CEST MRI for non-MR physicists. *EJNMMI Phys*. 2016;3:19.
2. Jones KM, Pollard AC, Pagel MD. Clinical applications of chemical exchange saturation transfer (CEST) MRI. *J Magn Reson Imaging*. 2018;47:11-27.
3. Longo DL, Bartoli A, Consolino L, et al. In vivo imaging of tumor metabolism and acidosis by combining PET and MRI-CEST pH imaging. *Cancer Res*. 2016;76:6463-6470.
4. Granja S, Tavares-Valente D, Queiros O, Baltazar F. Value of pH regulators in the diagnosis, prognosis and treatment of cancer. *Semin Cancer Biol*. 2017;43:17-34.
5. Parks SK, Chiche J, Pouysségur J. Disrupting proton dynamics and energy metabolism for cancer therapy. *Nat Rev Cancer*. 2013;13:611-623.
6. Kato Y, Ozawa S, Miyamoto C, et al. Acidic extracellular microenvironment and cancer. *Cancer Cell Int*. 2013;13:1-8.
7. Ma B, Blakeley JO, Hong X, et al. Applying amide proton transfer-weighted MRI to distinguish pseudoprogression from true progression in malignant gliomas. *J Magn Reson Imaging*. 2016;44:456-462.
8. Zhou J, Tryggestad E, Wen Z, et al. Differentiation between glioma and radiation necrosis using molecular magnetic resonance imaging of endogenous proteins and peptides. *Nat Med*. 2011;17:130-134.
9. Mehrabian H, Desmond KL, Soliman H, Sahgal A, Stanisz GJ. Differentiation between radiation necrosis and tumor progression using chemical exchange saturation transfer. *Clin Cancer Res*. 2017;23:3667-3675.
10. Randtke EA, Granados JC, Howison CM, Pagel MD, Cárdenas-Rodríguez J. Multislice CEST MRI improves the spatial assessment of tumor pH. *Magn Reson Med*. 2017;78:97-106.
11. Bai Y, Lin Y, Zhang W, et al. Noninvasive amide proton transfer magnetic resonance imaging in evaluating the grading and cellularity of gliomas. *Oncotarget*. 2017;8:5834-5842.
12. Otazo R, Lambin P, Pignol JP, et al. MRI-guided radiation therapy: an emerging paradigm in adaptive radiation oncology. *Radiology*. 2021;298:248-260.
13. Heo H-Y, Han Z, Jiang S, Schär M, van Zijl PC, Zhou J. Quantifying amide proton exchange rate and concentration in chemical exchange saturation transfer imaging of the human brain. *Neuroimage*. 2019;189:202-213.
14. Zhou Z, Han P, Zhou B, et al. Chemical exchange saturation transfer fingerprinting for exchange rate quantification. *Magn Reson Med*. 2018;80:1352-1363.
15. Cohen O, Huang S, McMahon MT, Rosen MS, Farrar CT. Rapid and quantitative chemical exchange saturation transfer (CEST) imaging with magnetic resonance fingerprinting (MRF). *Magn Reson Med*. 2018;80:2449-2463.
16. McMahon MT, Gilad AA, Zhou J, Sun PZ, Bulte JW, van Zijl PC. Quantifying exchange rates in chemical exchange saturation transfer agents using the saturation time and saturation power dependencies of the magnetization transfer effect on the magnetic resonance imaging signal (QUEST and QUESP): pH calibration for poly-L-lysine and a starburst dendrimer. *Magn Reson Med off J Int Soc Magn Reson Med*. 2006;55:836-847.
17. Randtke EA, Chen LQ, Corrales LR, Pagel MD. The Hanes-Woolf linear QUESP method improves the measurements of fast chemical exchange rates with CEST MRI. *Magn Reson Med*. 2014;71:1603-1612.
18. Zaiss M, Angelovski G, Demetriou E, McMahon MT, Golay X, Scheffler K. QUESP and QUEST revisited–fast and accurate quantitative CEST experiments. *Magn Reson Med*. 2018;79:1708-1721.
19. Van Zijl PC, Zhou J, Mori N, Payen J-F, Wilson D, Mori S. Mechanism of magnetization transfer during on-resonance water saturation. A new approach to detect mobile proteins, peptides, and lipids. *Magn Reson Med Off J Int Soc Magn Reson Med*. 2003;49:440-449.
20. Ma D, Gulani V, Seiberlich N, et al. Magnetic resonance fingerprinting. *Nature*. 2013;495:187-192.
21. Kang B, Kim B, Schär M, Park H, Heo H-Y. Unsupervised learning for magnetization transfer contrast MR fingerprinting: application to CEST and nuclear Overhauser enhancement imaging. *Magn Reson Med*. 2021;85:2040-2054.
22. Kim B, Schär M, Park H, Heo H-Y. A deep learning approach for magnetization transfer contrast MR fingerprinting and chemical exchange saturation transfer imaging. *Neuroimage*. 2020;221:117165.
23. Z. Zhou, Q. Yang, Z. Fan, P. Han, and D. Li, "CEST fingerprinting: initial study in human subjects," in Proceedings of the International Society of Magnetic Resonance in Medicine, Paris, France, 2018, p. 0417.
24. O. Perlman, C. T. Farrar, and O. Cohen, "Deep learning global schedule optimization for chemical exchange saturation transfer MR fingerprinting (CEST-MRF)," in Proceedings of the International Society of Magnetic Resonance in Medicine, Virtual Conference, p. 3576.
25. Perlman O, Herz K, Zaiss M, Cohen O, Rosen MS, Farrar CT. CEST MR-fingerprinting: practical considerations and insights for acquisition schedule design and improved reconstruction. *Magn Reson Med*. 2020;83:462-478.
26. Cohen O, Zhu B, Rosen MS. MR fingerprinting deep reconstruction network (DRONE). *Magn Reson Med*. 2018;80:885-894.
27. Perlman O, Ito H, Herz K, et al. Quantitative imaging of apoptosis following oncolytic virotherapy by magnetic resonance fingerprinting aided by deep learning. *Nat Biomed Eng*. 2022;6:648-657.
28. O. Cohen, C. T. Farrar, B. Zhu, and M. S. Rosen, "Fast deep-learning reconstruction of highly multi-dimensional MR fingerprinting data," Presented at the ISMRM Machine Learning Workshop, Pacific Grove, California, 2018.
29. O. Perlman, O. Cohen, S. Huang, et al., "Proton exchange rate, volume fraction, T1, and T2 MR fingerprinting using an optimized acquisition schedule and a deep RecOnstruction NEtwork (DRONE)," Presented at the 7th International Workshop on Chemical Exchange Saturation Transfer Imaging, Beijing, China, Nov. 2018.

30. O. Perlman O Cohen H Ito et al., "Sequential and deep multi-Pool CEST MR fingerprinting in in-vivo tumor-bearing mice," Presented at the 27th Annual Meeting, International Society of Magnetic Resonance in Medicine, Paris, France, May 2019.
31. Paszke A, Gross S, Massa F, et al. Pytorch: an imperative style, high-performance deep learning library. *Adv Neural Inf Process Syst*. 2019;32:8026-8037.
32. Park J-S. Optimal Latin-hypercube designs for computer experiments. *J Stat Plan Inference*. 1994;39:95-111.
33. D. P. Kingma and J. Ba, "Adam: a method for stochastic optimization," Presented at the 3rd International Conference on Learning Representations, ICLR, San Diego, CA, USA,May 2015.
34. Collins DL, Zijdenbos AP, Kollokian V, et al. Design and construction of a realistic digital brain phantom. *IEEE Trans Med Imaging*. 1998;17:463-468.
35. Cohen O, Rosen MS. Algorithm comparison for schedule optimization in MR fingerprinting. *Magn Reson Imaging*. 2017;41:15-21.
36. P. K. Mudrakarta, A. Taly, M. Sundararajan, and K. Dhamdhere, "Did the model understand the question?," ArXiv Prepr. ArXiv180505492, 2018.
37. M. Sundararajan, A. Taly, and Q. Yan, "Axiomatic attribution for deep networks," in International Conference on Machine Learning, 2017, pp. 3319–3328.
38. Lawrence I, Lin K. A concordance correlation coefficient to evaluate reproducibility. *Biometrics*. 1989;45(1):255-268.
39. Bagga P, Crescenzi R, Krishnamoorthy G, et al. Mapping the alterations in glutamate with Glu CEST MRI in a mouse model of dopamine deficiency. *J Neurochem*. 2016;139:432-439.
40. Ellingson BM, Bendszus M, Boxerman J, et al. Consensus recommendations for a standardized brain tumor imaging protocol in clinical trials. *Neuro-Oncol*. 2015;17:1188-1198.
41. Tukey JW. Comparing individual means in the analysis of variance. *Biometrics*. 1949;5:99-114.
42. Perlman O, Ito H, Herz K, et al. Quantitative imaging of apoptosis following oncolytic virotherapy by magnetic resonance fingerprinting aided by deep learning. *Nat Biomed Eng*. 2021;6:648-657.
43. Bojorquez JZ, Bricq S, Acquitter C, Brunotte F, Walker PM, Lalande A. What are normal relaxation times of tissues at 3 T? *Magn Reson Imaging*. 2017;35:69-80.
44. Lu H, Nagae-Poetscher LM, Golay X, Lin D, Pomper M, Van Zijl PC. Routine clinical brain MRI sequences for use at 3.0 tesla. *J Magn Reson Imaging Off J Int Soc Magn Reson Med*. 2005;22:13-22.
45. Stanisz GJ, Odrobina EE, Pun J, et al. T1, T2 relaxation and magnetization transfer in tissue at 3T. *Magn Reson Med Off J Int Soc Magn Reson Med*. 2005;54:507-512.
46. Lee PK, Watkins LE, Anderson TI, Buonincontri G, Hargreaves BA. Flexible and efficient optimization of quantitative sequences using automatic differentiation of Bloch simulations. *Magn Reson Med*. 2019;82:1438-1451.
47. Sommer K, Amthor T, Doneva M, Koken P, Meineke J, Börnert P. Towards predicting the encoding capability of MR fingerprinting sequences. *Magn Reson Imaging*. 2017;41:7-14.
48. Zhao B, Haldar JP, Liao C, et al. Optimal experiment design for magnetic resonance fingerprinting: Cramer-Rao bound meets spin dynamics. *IEEE Trans Med Imaging*. 2018;38:844-861.
49. O. Cohen, "MR fingerprinting schedule optimization network (MRF-SCONE)," in Proceedings of the International Society of Magnetic Resonance in Medicine, Montreal, May 11–May 16, p. 4531.
50. Cadoux-Hudson T, Rajagopalan B, Ledingham J, Radda G. Rapid communication: response of the human brain to a hypercapnic acid load in vivo. *Clin Sci*. 1990;79:1-3.
51. Wen Z, Hu S, Huang F, et al. MR imaging of high-grade brain tumors using endogenous protein and peptide-based contrast. *Neuroimage*. 2010;51:616-622.
52. Grossman R, Tyler B, Brem H, et al. Growth properties of SF188/V + human glioma in rats in vivo observed by magnetic resonance imaging. *J Neurooncol*. 2012;110:315-323.
53. Zhou J, Zaiss M, Knutsson L, et al. Review and consensus recommendations on clinical APT-weighted imaging approaches at 3T: application to brain tumors. *Magn Reson Med*. 2022;88:546-574.
54. Zaiss M, Windschuh J, Paech D, et al. Relaxation-compensated CEST-MRI of the human brain at 7 T: unbiased insight into NOE and amide signal changes in human glioblastoma. *Neuroimage*. 2015;112:180-188.
55. Zaiss M, Schuppert M, Deshmane A, et al. Chemical exchange saturation transfer MRI contrast in the human brain at 9.4 T. *Neuroimage*. 2018;179:144-155.
56. Zhou J, Heo H-Y, Knutsson L, van Zijl PC, Jiang S. APT-weighted MRI: techniques, current neuro applications, and challenging issues. *J Magn Reson Imaging*. 2019;50:347-364.
57. Lagadic-Gossmann D, Huc L, Lecureur V. Alterations of intracellular pH homeostasis in apoptosis: origins and roles. *Cell Death Differ*. 2004;11:953-961.
58. Nilsson C, Johansson U, Johansson A-C, Kågedal K, Öllinger K. Cytosolic acidification and lysosomal alkalinization during TNF-α induced apoptosis in U937 cells. *Apoptosis*. 2006;11:1149-1159.
59. Webb BA, Chimenti M, Jacobson MP, Barber DL. Dysregulated pH: a perfect storm for cancer progression. *Nat Rev Cancer*. 2011;11:671-677.
60. O. Cohen, R. J. Young, C. T. Farrar, and R. Otazo, "Fast CEST MR fingerprinting with increased volumetric coverage using slice permuted acquisition and deep learning reconstruction," in Proceedings of the International Society of Magnetic Resonance in Medicine, 2022, p. 0563.
61. Cohen O, Polimeni JR. Optimized inversion-time schedules for quantitative T1 measurements based on high-resolution multi-inversion EPI. *Magn Reson Med*. 2018;79:2101-2112.

SUPPORTING INFORMATION

Additional supporting information may be found in the online version of the article at the publisher's website.

Supporting Information Table S1: Tissue parameter values of the digital phantom used

Supporting Information Table S2: Tissue parameter ranges used in the training dataset and dictionary generation. Dictionary parameters bounds are formatted as lower:interval:upper

Supporting Information Figure S1: DM reconstruction of 6 parameters in a digital phantom in comparison

to the reference values. The ranges used to generate the 4 million dictionary entries are shown in Table S2. Regions associated with the background, skull and scalp were set to zero. The error, calculated as $100 \times |\text{Reference} - \text{DM}|/\text{Reference}$, is shown for each tissue. The DM reconstruction resulted in a larger error due to the relatively sparse coverage of the tissue parameter space provided by the dictionary

Supporting Information Figure S2: Synthesized Z spectra generated from the CEST-MRF tissue parameters for a baseline set of values and 2× and 0.5× multiples of the parameters. The differences between the baseline and the other spectra are shown by the dashed curves along with the corresponding Pearson correlation and RMSE. (A-B) WM and GM spectra for the CEST (i.e. ksw, fs) parameters. (C-D) WM and GM spectra for the MT (i.e. kssw, fss) parameters

Supporting Information Figure S3: (A) Comparison between the measured and DRONE synthesized CEST-MRF fingerprints for a WM voxel. (B) Comparison between the measured and synthesized fingerprints for a GM voxel. (C-F) Synthesized CEST-MRF fingerprints for a baseline set of values and 2× and 0.5× multiples of the CEST or MT parameters for WM or GM. The differences between the baseline and the other spectra are shown by the dashed curves along with the corresponding Pearson correlation and RMSE. Each of the synthetic fingerprints were generated for a change of one parameter at a time with all others held constant. The measured fingerprints include changes in all parameters simultaneously and may include contributions from partial volume, slice profile effects, flow/motion, receiver sensitivity etc. not modeled here. Note that because it is trained on synthetic fingerprints, the DRONE network is nevertheless able to 'see-through' these confounding factors to yield the correct maps

Supporting Information Table S3: Regression model coefficients used to measure the impact of the other tissue parameters on the CEST parameters ksw and fs. Note that for both ksw and fs the effect of the MT parameters (kssw, fss) is an order of magnitude smaller than that of other factors illustrating the independence of the CEST parameters from MT

Supporting Information Figure S4: The mean absolute error in each tissue parameter for repeated applications of the DRONE reconstruction in comparison to repeated applications of DM. An initial set of tissue parameters reconstructed from a healthy subject was used to synthesize a numerical phantom and simulate a CEST-MRF acquisition. The synthetic fingerprints were reconstructed with DM or the DRONE network and the process repeated 40 times (index starts at 0) to test the self-consistency of each method. For sufficiently large iterations, the error in all parameters converged to ∼0% for the DRONE network but not for DM. The DRONE network's initial reconstruction error was also notably smaller for all parameters

Supporting Information Figure S5: (A) Dictionary matched reconstruction of the in vivo healthy subject data. The ranges used to generate the 4 million dictionary entries are shown in Table S2. While large, the dictionary size used (4 million entries), is insufficient to cover the 7-dimensional space of tissue parameters leading to the heavily discretized and noisy appearance of the maps, unlike the equivalent DRONE reconstruction shown in Figure 4. (B) Dictionary reconstruction of the tumor patient, showing similarly discretized and noisy appearance

How to cite this article: Cohen O, Yu VY, Tringale KR, et al. CEST MR Fingerprinting (CEST-MRF) for Brain Tumor Quantification Using EPI Readout and Deep Learning Reconstruction. *Magn Reson Med*. 2022;1-17. doi: 10.1002/mrm.29448

WOULD YOU LIKE TO POST AN INFORMAL COMMENT ABOUT THIS PAPER, OR ASK THE AUTHORS A QUESTION ABOUT IT?

If so, please visit https://mrm.ismrm.org/ and register for our Magn Reson Med Discourse site (registration is free).

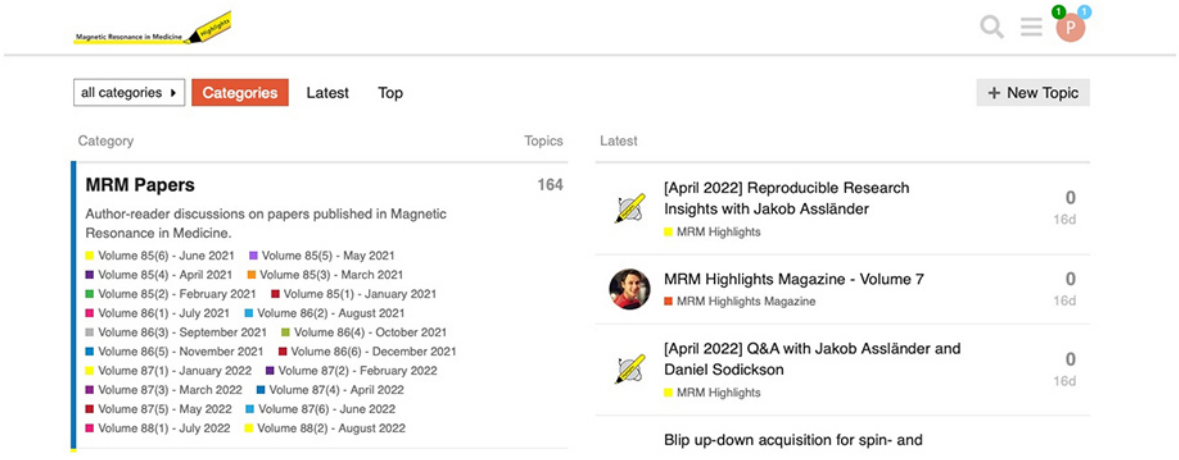

Magn Reson Med is currently listing the top 8 downloaded papers from each issue (including Editor's Picks) for comments and questions on the Discourse web site.

However, we are happy to list this or any other papers (please email mrm@ismrm.org to request the posting of any other papers.)

We encourage informal comment and discussion about Magn Reson Med papers on this site. Please note, however, that a formal errata from the authors should still be submitted in the usual way via our Manuscript Central online submission system.